THEMIS observations of particle acceleration by a magnetosheath jet-driven bow wave

Terry Z. Liu[1], Heli Hietala[1,2], Vassilis Angelopoulos[1], Yuri Omelchenko[3], Vadim Roytershteyn[3], and Rami Vainio[2]

[1]University of California, Los Angeles, USA
[2]University of Turku, Finland
[3]Space Science Institute, USA

Abstract

Localized magnetosheath jets with high dynamic pressure are frequently observed downstream of Earth's bow shock. When such a fast magnetosheath jet compresses the ambient magnetosheath plasma, an earthward compressional bow wave could form. Such bow waves have been predicted by simulations but have never been observed. Using multipoint THEMIS observations, we report the first observation where such a bow wave driven by an intrinsically-formed magnetosheath jet can reflect and accelerate particles up to tens of keV for ions and 100 keV for electrons. By analyzing the ion distributions, we infer how particles reach the spacecraft from the bow wave demonstrating good agreement with our model of single particle motion. Our study implies that particle acceleration at magnetosheath jets could contribute significantly to particle acceleration at shocks in general.

1. Introduction

Magnetosheath jets are nonlinear transient phenomena observed downstream of Earth's bow shock. They are characterized by large dynamic pressure (>0.5 solar wind dynamic pressure) (see review Plaschke et al., 2018 and the references therein) and typically have enhanced velocity and density with spatial scale in ~1 R_E (e.g., Plaschke et al., 2016). Magnetosheath jets occur at or downstream of the quasi-parallel bow shock much more frequently than in the case of the quasi-perpendicular bow shock (e.g., Plaschke et al., 2013). Because the quasi-parallel bow shock is structured and rippled, the shock surface has different inclinations at different locations (e.g., Karimabadi et al, 2014; Gingell et al., 2017). At the spots where the shock surface is tilted, the downstream plasma is less decelerated and less thermalized, forming magnetosheath jets (e.g., Hietala et al., 2009; Hietala et al., 2013). In a minority of cases, magnetosheath jets can also be driven by upstream drivers, such as solar wind discontinuities (Archer et al., 2012) and foreshock transients (Archer et al., 2014; Omidi et al., 2016).

Simulations of Karimabadi et al (2014) suggested that magnetosheath jets may have global consequences in the geospace environment. Observations by Hietala et al. (2018) confirmed that they can compress the magnetopause and trigger reconnection. Archer et al. (2019) found that they can excite eigenmodes of the magnetopause surface. They can also drive compressional low frequency waves within the magnetosphere, ionospheric flow enhancements, and auroral brightening (e.g., Hietala et al., 2012; Archer et al., 2013; Wang et al., 2018).

Hietala et al. (2009; 2012) found that while the supermagnetosonic magnetosheath jet pushed the magnetopause earthwards, it formed a weak secondary shock (sunward in the plasma frame). When a fast magnetosheath jet compresses the ambient plasma, earthward compressional waves are created. Jet-driven bow waves reported in simulations (e.g., Karimabadi et al., 2014) may steepen into a shock given enough time and space to evolve. Such fast-mode bow waves could also form in response to propagating flux transfer events (FTEs) from magnetopause reconnection (Jarvinen et al., 2018). These bow waves are capable of accelerating ions, similar to shocks. Consequently, we seek to examine the possible presence and properties of jet-driven bow waves to understand their contribution to downstream particle energization.

Using multipoint Time History of Events and Macroscale Interactions during Substroms (THEMIS) observations, we report the first observations of a jet-driven bow wave. We show that there are indeed accelerated ions and electrons at this bow wave and explain how they arrive at the spacecraft by analyzing the particle distributions.

2. Data

We used data from the THEMIS mission probes in 2008 (Angelopoulos, 2008). In the first two dayside seasons of that mission (Sibeck and Angelopoulos, 2008), TH-B (~30 R_E apogee) and TH-C (~20 R_E apogee) were often in the solar wind, whereas TH-D and TH-E (~10 R_E apogee) were often in the magnetosheath. We analyzed plasma data from the electrostatic analyzer (ESA) (McFadden et al., 2008) and the solid state telescope (SST) (Angelopoulos, 2008) and magnetic field data from the fluxgate magnetometer (Auster et al., 2008).

We search the event list reported by Plaschke et al. (2013) for magnetosheath jets that have a bow wave or shock-like structure ahead of them. We find 364 events (out of 2859) where magnetosheath jets in the spacecraft frame are supermagnetosonic, and there is a magnetic field strength and density enhancement ahead of each jet, as well as a change in the plasma flow direction (see supporting information for detailed criteria). Here we present one event that features two THEMIS spacecraft in the solar wind and two THEMIS spacecraft in the magnetosheath observing the jet (Figure 1a, b) in fast survey mode (higher time resolution and angular resolution than slow survey mode) under stable solar wind conditions without drivers.

3. Results

Figure 1a-b shows the THEMIS spacecraft locations during the event on Sep 25, 2008. TH-B and TH-C were in the solar wind near the bow shock. (In Figure 1, TH-B, C appear to be in the magnetosheath, because of the projection and the uncertainty of the bow shock model.) Figure 1c-f shows a very stable solar wind condition indicating that there were no solar wind driver discontinuities or upstream foreshock transients. Because solar wind B_x is very small (see arrows in Figure 1a,b and blue lines in Figure 1c,d), TH-D and TH-E (separated from each other by ~1 R_E; and from the magnetopause by ~0.6 and 0.1 R_E, respectively) observed a magnetosheath jet downstream of the quasi-perpendicular bow shock (Figure 2). The dynamic pressure within the jet exceeded one half of the solar wind dynamic pressure (Figure 2h at ~15:13:20 UT and Figure 2p ~15:14:20 UT, respectively), satisfying our definition of a jet. There was another magnetosheath jet earlier during the time interval shown in Figure 2, but it is not related to this study.

At the leading edge of the magnetosheath jet, TH-D observed a shock-like structure with increases in both magnetic field strength and density (magenta in Figure 2a, b). We calculate that the shock normal n=[-0.36, 0.90, -0.11] in GSE with uncertainty 7.6° using the mixed-mode coplanarity method and [-0.13, 0.96, -0.15] with uncertainty 7.5° using the magnetic-mode coplanarity method with the data upstream and downstream of the shock-like structure (Schwartz, 1998; using time interval around yellow in Figure 2a – c) corresponding to a local θ_{Bn} of $56.2° \pm 5.8°$. Note that the normal, calculated using the minimum variance analysis method (MVA; Sonnerup and Scheible, 1998), is [0.84, -0.53, -0.01], with uncertainty 4.2° and a minimum to intermediate eigenvalue ratio of ~0.1. Here we use the normal from the mixed-mode coplanarity method in the following calculations. We calculate the shock normal speed in the spacecraft frame, $V_{sh}^{sc} = 111 \pm 10$ km/s earthward, using conservation of the mass flux (Schwartz, 1998). The upstream flow speed in the shock normal incidence frame is 156 ± 18 km/s, faster than the local fast wave speed 147 ± 1 km/s. However, the Mach number is only

1.06 ± 0.12, and ion heating is not pronounced (for details see supporting information). It may be a fast-mode wave in the process of steepening into a shock. Here we simply call it bow wave. Ahead of the bow wave, there is a train of linearly polarized magnetosonic waves propagating nearly perpendicular to the magnetic field (see Figure S1). The plasma beta ahead of the jet is 8.0 ± 1.2, and the corresponding critical Mach number is ~1 to 1.1 (Edmiston and Kennel, 1984).

TH-E also observed this structure, but the magnetic field strength and density enhancements across it did not occur at the same time but with a time delay of ~5 s (magenta in Figure 2i – p). One possible reason for that is that the structure of the jet-driven bow wave was perturbed by another transient ahead of it (labeled in Figure 2i, see supporting information). We will estimate the bow wave normal based on how TH-E crossed the jet later in this Section.

Right upstream of the jet-driven bow wave, both spacecraft observed some suprathermal ions (from several keV up to tens of keV at around 15:12 to 15:13 UT in Figure 2d,e and around 15:13 to 15:14 UT in Figure 2l,m, respectively) and electrons (up to over 100 keV at around 15:13 UT in Figure 2f and 15:14 UT in Figure 2n, respectively) with energies higher than the ambient magnetosheath plasma. Downstream of the jet-driven bow wave, an ion energy dispersion from several to tens of keV was also observed at both spacecraft (~15:13:15-15:13:30 UT in Figure 2e and ~15:14:15-15:14:30 UT in Figure 2m, respectively).

To investigate whether these particles originated from the bow wave, we analyze the particle spectrograms up and downstream of the jet-driven bow wave. We focus on the ions because the angular resolution of electron distributions was not good during this event. Figure 3 shows ion energy spectra in three directions: anti-parallel, perpendicular, and parallel to the spin-averaged (3 s) magnetic field at both spacecraft. In the background magnetosheath at the beginning of the time interval, there were just thermal ions. When the two spacecraft approached the jet-driven bow wave, they first observed suprathermal ions mainly in the anti-parallel direction with dispersion at ~15:12:20 UT for TH-D (Figure 3b) and ~15:13:00 UT for TH-E (Figure 3f), respectively. When the two spacecraft were near the jet-driven bow wave, suprathermal ions became very isotropic (~15:13:00 UT in Figure 3d) or mainly in the parallel direction (~15:14:00 in Figure 3h) rather than in the anti-parallel direction. Downstream of the jet-driven bow wave, the dispersion is seen mainly in the perpendicular direction at both spacecraft (~15:13:30 UT in Figure 3c and 15:14:20 UT in Figure 3g, respectively).

To further understand the ion spectra and especially the dispersions, we analyze cuts of the ion distribution functions in various regions: Each column in Figure 4 corresponds to a vertical dashed line in Figure 3a-d. The distributions are shown both in the BV plane (where the horizontal axis is along the spin-averaged magnetic field and the vertical axis contains the bulk velocity) and in the GSE-XY plane. Sketches in Figure 5 illustrate the inferred event geometry and ion dynamics.

Figures 4a, and b show that the ion distributions in the background magnetosheath comprise only a single component. As TH-D approached the jet-driven bow wave, we see two components: a field-aligned ion beam in the anti-parallel direction with an $E \times B$ drift and the main magnetosheath ion population (Figure 4c, e, g). In the GSE-XY plane (Figure 4d, f, h), the field-aligned beam was moving along -GSE-X and -GSE-Y directions, meaning that these ions cannot come from the magnetopause due to magnetic reconnection or FTE, but originated from the sunward and dawnward direction, where the jet was also coming from (Figure 1a, Figure 5).

In Figure 4c, e, g, the minimum anti-parallel speed of the field-aligned beam decreased as the spacecraft was closer to the jet-driven bow wave, which corresponds to the anti-parallel dispersion in Figure 3b. We propose the following explanation for this dispersion: These ions reached the spacecraft along both the field-aligned (at $V_{\parallel}$) and $E \times B$ direction (at $V_{E\times B}$). The speed in the two directions satisfies $V_{\parallel}/d_{\parallel} = V_{E\times B}/d_{E\times B}$, where $d_{\parallel}$ and $d_{E\times B}$ are the distance between spacecraft and the bow wave in the field-aligned and $E \times B$ direction, respectively. If the spacecraft approached the bow wave mainly in the field-aligned direction, i.e., $d_{\parallel}$ decreased much faster than $d_{E\times B}$, ions needed smaller and smaller $V_{\parallel}$ with the constant $V_{E\times B}$ to reach the spacecraft (as sketched in Figure 5a). Following this idea, we fit the anti-parallel dispersion (dotted line in Figure 3b) by estimating the approaching speed between the spacecraft and the bow wave as ~200 km/s along the field line and 10 – 20 km/s along the $E \times B$ direction (for detailed equations see the supporting information). TH-D observed the dispersed ions first and TH-E observed them ~50 s later. Such a time difference is consistent with the distance between two spacecraft (~1 R_E) and the $E \times B$ drift speed (~120 km/s). However, we do not fit the anti-parallel dispersion at TH-E because the observed flux is not large enough to see a full beam (not shown here).

Another characteristic of these field-aligned ions is that the minimum field-aligned speed of the ions gyrating along the $E \times B$ direction was smaller than of those gyrating away from this direction (Figure 4c, e, g). A possible explanation is that if the jet-driven bow wave had a curved shape (in both XZ and YZ planes in Figure 5a,c), the guiding center of ions gyrating towards the spacecraft along the $E \times B$ direction (curved purple arrow) had a smaller field-aligned distance to the bow wave than that of ions gyrating away from this direction (curved magenta arrow). As already discussed, a smaller field-aligned distance to the bow wave means ions needed a smaller field-aligned speed to reach the spacecraft. This again supports the interpretation that the source of such suprathermal ions is the jet-driven bow wave.

As the distance between the jet-driven bow wave and spacecraft decreases, the direction of B_n will reverse if the bow wave is curved (Figure 5a). This causes accelerated ions to move in the parallel direction as observed at TH-E at ~15:14:00 UT in Figure 3h. At TH-D, there was a decrease in the anti-parallel flux at ~15:12:50 UT in Figure 3b, corresponding to the time of B_n reversal. Then ions became isotropic (Figure 4i, j), probably due to the waves observed near the jet-driven bow wave (at ~15:13:10 UT in Figure 3a).

Figure 4k shows that as the spacecraft crossed the jet-driven bow wave to the downstream side, suprathermal ions were mainly gyrating with a finite anti-parallel speed. A possible reason is that as the magnetic field was mainly in -GSE-Z roughly perpendicular to the bow wave normal, suprathermal ions from the jet-driven bow wave had to gyrate towards the spacecraft (Figure 5d). This would also explain the perpendicular dispersion: as the spacecraft moved away from the bow wave in the perpendicular direction, ions from the bow wave needed a larger gyroradius and thus larger gyrospeed to reach the spacecraft. Based on this idea, if we use the same relative speed between the bow wave and the spacecraft in the $E \times B$ direction estimated previously, 10 – 20 km/s, the calculated energy dispersion matches the observed spectra very well for both spacecraft (dotted line in Figure 3c, g; see equation in the supporting information). This again agrees with the interpretation that these ions originate from the bow wave.

Additionally, in the GSE-XY plane (Figure 4l), which is also the gyrophase plane as the magnetic field was mainly along -GSE-Z, the gyrospeed was a function of gyrophase. Ions with gyrophase in the third quadrant had larger gyrospeeds than those in the first quadrant (also seen in the ESA-SST combined distribution in Figure S2). A possible cause for this feature is sketched in Figure 5d showing the projected trajectories of gyrating ions with finite field-aligned velocities. For two ions with the same initial gyrophase, the one observed in the third quadrant (magenta) needed a larger gyroradius to reach the spacecraft than the one in the first quadrant (purple).

As the TH-E spacecraft should approach the bow wave along a similar trajectory as TH-D, we estimate the normal that should be observed by TH-E. Based on the observed field-aligned beam direction, we sketch the trajectories of two spacecraft in Figure 5a, b. We see that the normal crossed by TH-E should have mainly been in the GSE-X direction. Such a normal is consistent with the MVA calculation [-0.99, 0.13, 0.01] with a minimum to intermediate eigenvalue ratio of 0.09. It is also consistent with the observed magnetic field strength enhancement in GSE-Y and velocity variation mainly in GSE-X compared to the background magnetosheath before the transient structure (Figure 2i, k), based on the Rankine–Hugoniot relations. Because TH-D and TH-E crossed different part of the bow wave, we can estimate the size of the jet-driven bow wave. Assuming that the bow wave was spherical and using the time delay and the speed of approach, we find the radius of the bow wave to be ~1.5 $R_{E.}$ (Figure 5b; see details in the supporting information.)

Finally, let us discuss how these ions could have gained their energy. One possible mechanism is that the bow wave and possibly the wave train ahead of it create magnetic mirrors where ions can gradient B drift along the convection electric field, i.e., shock drift-like acceleration (e.g., Burgess et al., 2012). Additionally, as the bow wave is moving earthward, reflected ions in the spacecraft frame can also gain twice of the bow wave normal speed (see detailed calculation in the supporting information). After acceleration, ions within the loss cone leak downstream (e.g., Figure 4k, l) and the rest backstream along the field line (e.g., Figure 4c – j).

As for the 100 keV electrons, the reason why they were observed right upstream of the bow wave is most likely that their field-aligned speed $V_{\parallel} \gg V_{E\times B}$, which causes $d_{E\times B} \ll d_{\parallel}$.

Therefore, to observe them the two spacecraft need to be very close to the field lines connected to the bow wave. The electron acceleration mechanism, however, still needs further investigation, as that requires distribution measurements at a higher angular and energy resolution than was available for this event.

4. Conclusions and Discussion

For the first time, we observe a bow wave driven by an intrinsically-formed magnetosheath jet and demonstrate that it accelerates both ions and electrons. Here we summarize the observations and our interpretation. When the spacecraft approached the bow wave mainly in the field-aligned direction, ions from the jet-driven bow wave needed a progressively smaller field-aligned speed to reach the spacecraft, resulting in the observed dispersion in the anti-parallel direction. When the spacecraft reached the field lines directly connected to the jet-driven bow wave, 100 keV electrons were observed. After the spacecraft entered the downstream side, the ions showed a perpendicular dispersion because particles gyrating towards the spacecraft needed an increasing gyrovelocity to reach them as the spacecraft were receding from the bow wave. As this process does not require the jet-driven bow wave to fully steepen into a shock, it may be a common process which could be tested by a statistical study in the future.

Previously, Liu et al. (2016) have shown that upstream of large-scale (bow) shocks a localized foreshock transient structure can create a secondary shock that accelerates particles, hence forming a new foreshock. In this study, we show that downstream of large-scale shocks, there can also be localized transients with bow waves energizing particles. Clearly, the shock environment relevant for particle acceleration is not just the shock itself, but also the nonlinear structures both upstream and downstream of it. These nonlinear structures could play an important role in shock-driven particle acceleration and should therefore be included in shock models.

229

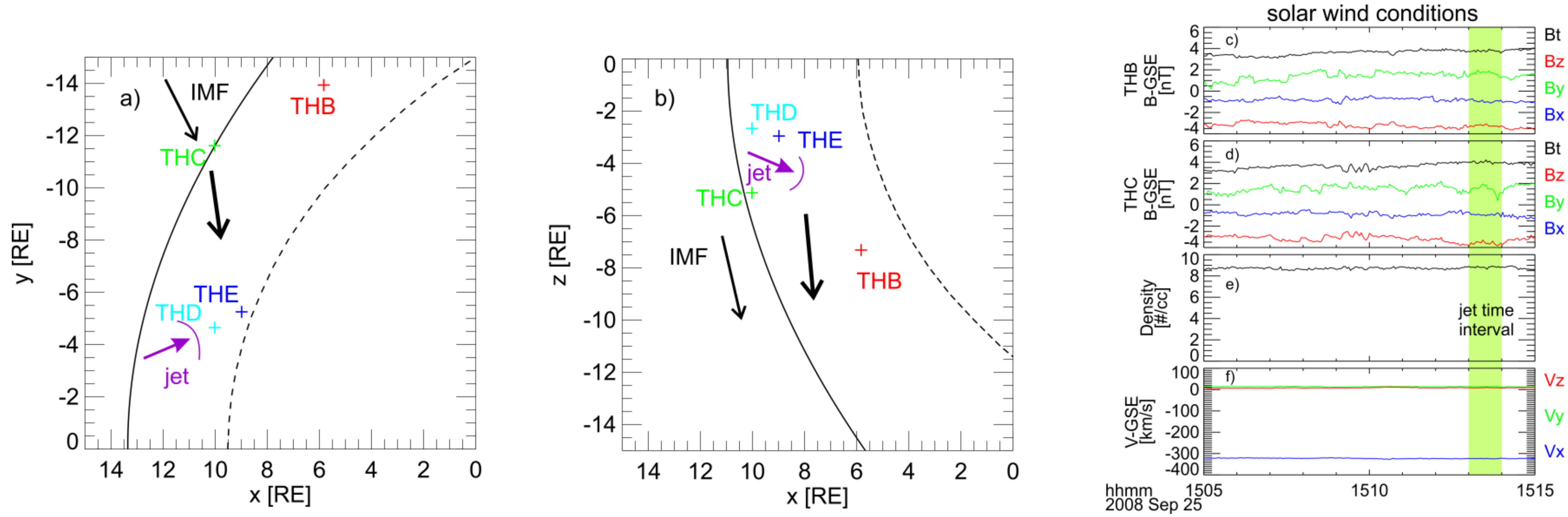

a)
IMF
THB
THC
THE
THD
jet
y [RE]
x [RE]
b)
THD
THE
jet
THC
IMF
THB
z [RE]
x [RE]
solar wind conditions
c)
THB B-GSE [nT]
Bt
Bz
By
Bx
d)
THC B-GSE [nT]
Bt
Bz
By
Bx
e)
Density [#/cc]
jet time interval
f)
V-GSE [km/s]
Vz
Vy
Vx
hhmm
2008 Sep 25
1505
1510
1515

Figure 1. (a) and (b) are THEMIS spacecraft position projected in the XY (z = -5 R_E) and XZ (y = -11 R_E) cuts (based on the position of TH-C). Solid curve indicates the bow shock position from Merka et al. (2005) model and dashed curve indicates the magnetopause position from Shue et al. (1998) model. Black arrows indicate IMF direction measured by TH-B and TH-C and magnetic field direction in the magnetosheath by TH-D. Purple arrow indicates the jet flow direction measured by TH-D. Right hand side shows the solar wind observations from TH-B, C: (c) TH-B and (d) TH-C observations of magnetic field in GSE (XYZ, total in blue, green, red, and black respectively); (e) TH-C observation of ion density; (f) TH-C observation of solar wind velocity in GSE.

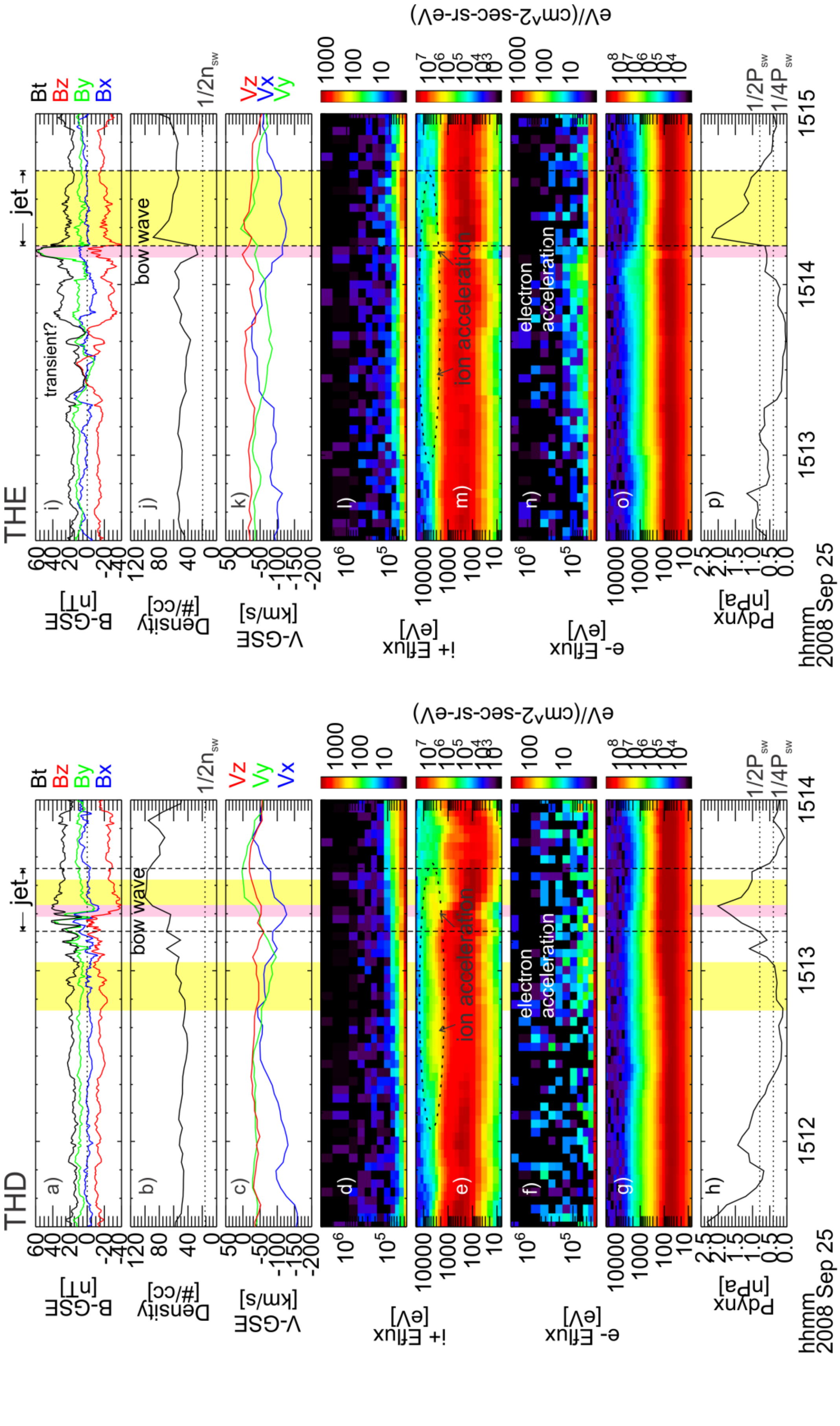
THD
THE
jet
bow wave
transient?
ion acceleration
electron acceleration
B-GSE [nT]
Density [#/cc]
V-GSE [km/s]
i+ Eflux [eV]
e- Eflux [eV]
Pdynx [nPa]
Bt
Bz
By
Bx
Vz
Vy
Vx
1/2n_sw
1/2P_sw
1/4P_sw
eV/(cm^2-sec-sr-eV)
hhmm
2008 Sep 25
1512
1513
1514
1515

Figure 2. Overview plots of TH-D (left) and TH-E (right) magnetosheath observations. In TH-D observations from top to bottom: (a) magnetic field in GSE; (b) ion density (dotted line indicates one half of the solar wind density); (c) ion bulk velocity in GSE; (d) ion energy flux spectrum from 30 keV to 700 keV; (e) ion energy flux spectrum from 7 eV to 25 keV (the accelerated ions are labeled with a dashed ellipse); (f) electron energy flux spectrum from 30 keV to 700 keV; (g) electron energy flux spectrum from 7 eV to 25 keV; (h) dynamic pressure in GSE-X (dotted lines indicate 1/2 and 1/4 of solar wind dynamic pressure, respectively). Vertical dashed lines indicate the time interval of the magnetosheath jet. Magenta region indicates the bow wave driven by the magnetosheath jet. Yellow regions indicate the upstream and downstream region used to calculate the parameters. TH-E observations are in the same format as TH-D observations except yellow region indicates the magnetosheath jet.

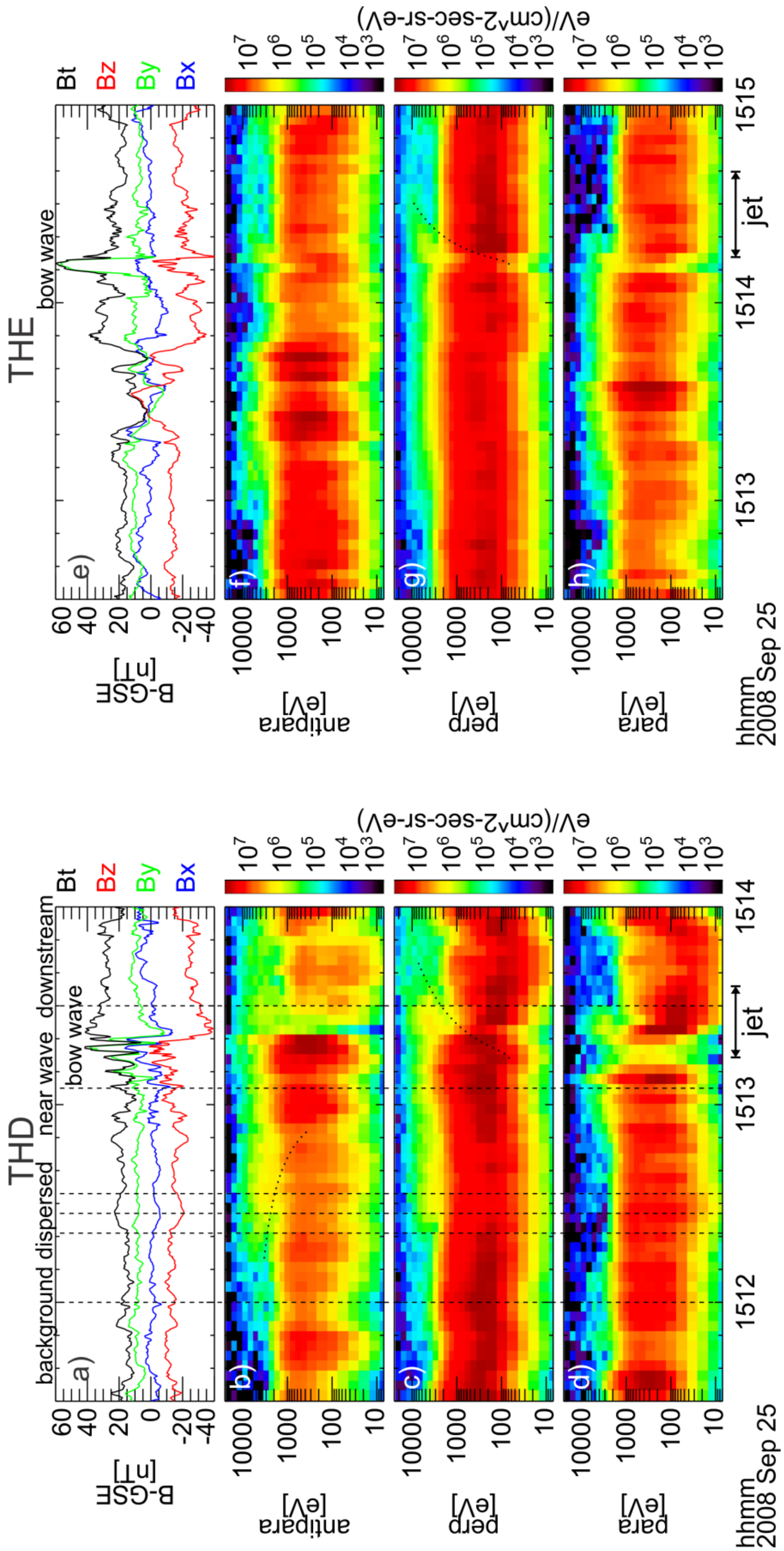

THD
THE
background dispersed
near wave
bow wave
downstream
jet
B-GSE [nT]
antipara [eV]
perp [eV]
para [eV]
Bt
Bz
By
Bx
eV/(cm^2-sec-sr-eV)
hhmm
2008 Sep 25
1512
1513
1514
1515

Figure 3. TH-D and TH-E observations of ion energy flux spectra in three directions. In TH-D observations from top to bottom: (a) magnetic field in GSE; (b) – (d) ion energy flux spectra in directions anti-parallel, perpendicular, and parallel to the magnetic field, respectively. Vertical dashed lines indicate the time of ion distributions shown in Figure 4. TH-E observations are in the same format as TH-D observations. Dotted curves in panels (b), (c), and (g) are fitted energy dispersion.

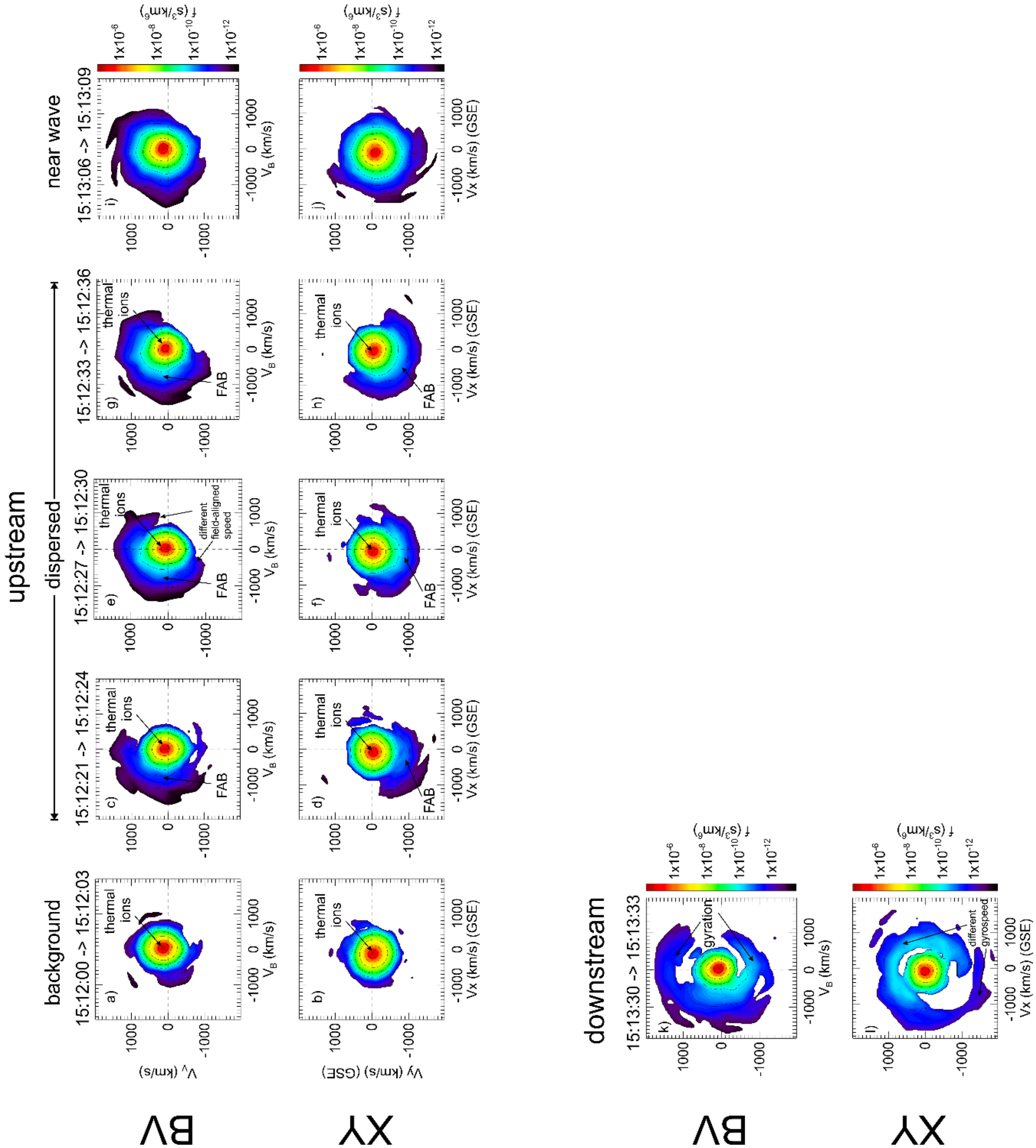

Figure 4. TH-D observations of ion distributions in various regions corresponding to the vertical dashed lines in Figure 3. Upper row is in BV plane (X axis is along the spin-averaged field line and Y axis contains the bulk velocity). Bottom row is in GSE-XY plane. FAB is short for field-aligned beam.

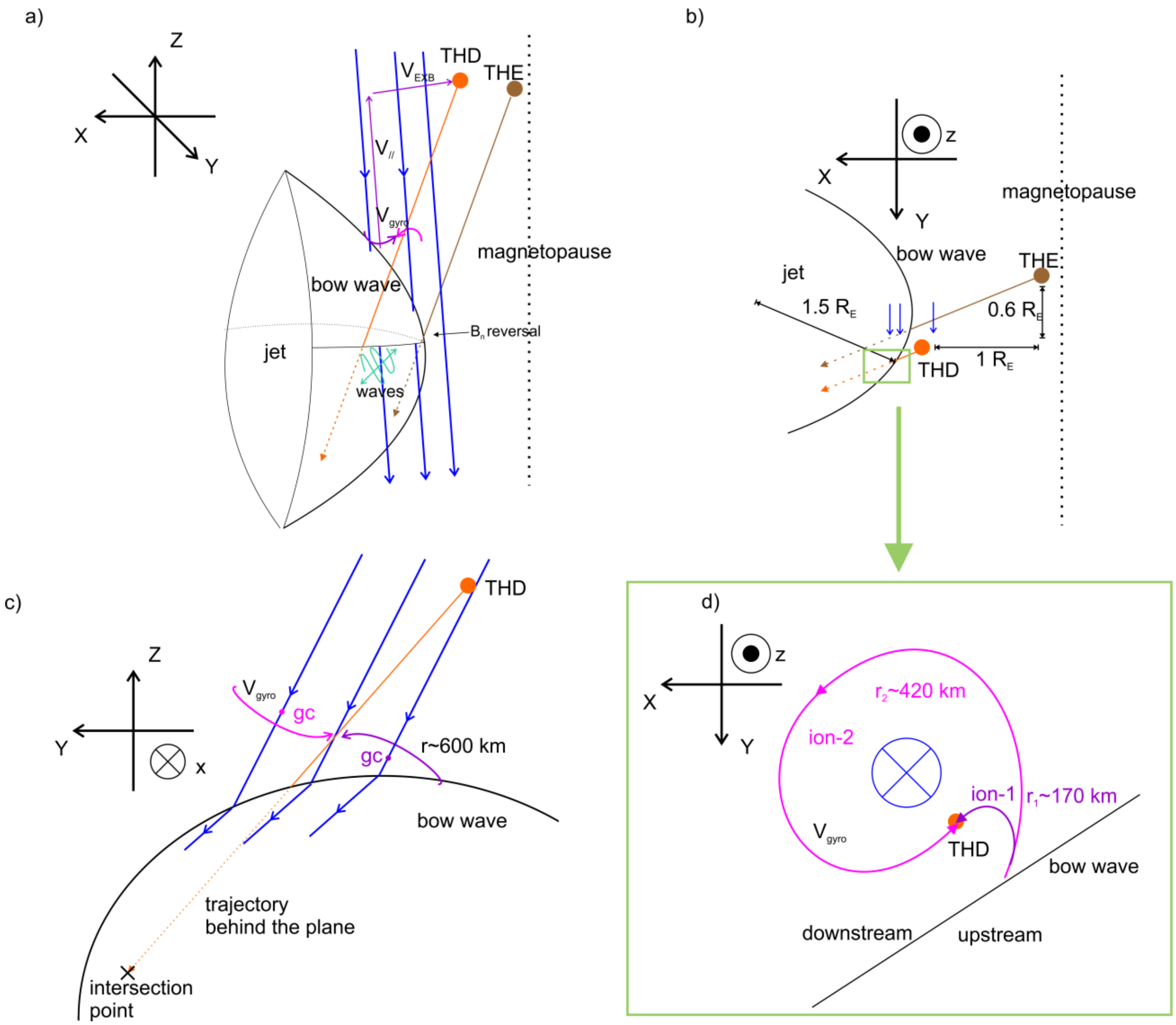

Figure 5. The sketches of the event in 3D (a), XY plane (b), XZ plane (c), and zoomed in near the bow wave in XY plane (d; corresponding to the green box in b). GC is short for guiding center. Blue arrows indicate the magnetic field direction. Orange and brown arrows indicate the approaching trajectory of TH-D and TH-E, respectively. Magenta and purple lines indicate the trajectory of ions reaching the spacecraft. Dark green lines in (a) indicate waves. Note that the spacecraft trajectory is more complicated than a straight line because of the evolution and curved shape of the bow wave.

Acknowledgements

The work at UCLA and SSI was supported by NASA grant NNX17AI45G. HH is supported by the Turku Collegium for Science and Medicine. The work in the University of Turku was performed in the framework of the Finnish Centre of Excellence in Research of Sustainable Space. RV acknowledges the financial support of the Academy of Finland (projects 309939 and 312357). We thank the THEMIS software team and NASA's Coordinated Data Analysis Web (CDAWeb, http://cdaweb.gsfc. nasa.gov/) for their analysis tools and data access. The THEMIS data and THEMIS software (TDAS, a SPEDAS v3.1 plugin, see Angelopoulos et al. (2019)) are available at http://themis.ssl.berkeley.edu.

References

Angelopoulos, V. (2008), The THEMIS mission, Space Sci. Rev., 141, 5–34, doi:10.1007/s11214-008-9336-1.

Angelopoulos, V., Cruce, P., Drozdov, A. et al. Space Sci Rev (2019) 215: 9. https://doi.org/10.1007/s11214-018-0576-4

Archer, M.O., T.S. Horbury, J.P. Eastwood (2012), Magnetosheath pressure pulses: Generation downstream of the bow shock from solar wind discontinuities. J. Geophys. Res. 117, 05228. doi:10.1029/2011JA017468

Archer, M.O., T.S. Horbury, J.P. Eastwood, J.M. Weygand, T.K. Yeoman, Magnetospheric response to magnetosheath pressure pulses: a low-pass filter effect. J. Geophys. Res. 118, 5454–5466 (2013). https://doi.org/10.1002/jgra.50519

Archer, M. O., Turner, D. L., Eastwood, J. P., Horbury, T. S., & Schwartz, S. J. (2014). The role of pressure gradients in driving sunward magnetosheath flows and magnetopause motion. Journal of Geophysical Research: Space Physics, 119, 8117–8125. https://doi.org/10.1002/2014JA020342

Archer, M. O., H. Hietala, M. D. Hartinger, F. Plaschke & V. Angelopoulos (2019). Direct observations of a surface eigenmode of the dayside magnetopause. Nat. Commun., 10, 615

Auster, H. U., et al. (2008), The THEMIS fluxgate magnetometer, Space Sci. Rev., 141, 235–264, doi:10.1007/s11214-008-9365-9.

Burgess, D., E. Möbius, and M. Scholer (2012), Ion acceleration at the Earth's bow shock, Space Sci. Rev., 173(1–4), 5–47, doi:10.1007/s11214-012-9901-5.

Edmiston JP, Kennel CF (1984), A parametric survey of the first critical Mach number for a fast MHD shock. J Plasma Phys 32:429–441

Gingell, I., Schwartz, S. J., Burgess, D., Johlander, A., Russell, C. T., Burch, J. L., …Wilder, F. (2017). MMS observations and hybrid simulations of surface ripples at a marginally quasi-parallel shock. Journal of Geophysical Research: Space Physics, 122, 11,003–11,017. https://doi.org/10.1002/2017JA024538

Hietala, H., T. V. Laitinen, K. Andréeová, R. Vainio, A. Vaivads, M. Palmroth, T. I. Pulkkinen, H. E. J. Koskinen, E. A. Lucek, and H. Rème (2009), Supermagnetosonic jets behind a collisionless quasiparallel shock, Phys. Rev. Lett., 103, 245,001, doi:10.1103/PhysRevLett.103.245001.

Hietala, H., N. Partamies, T. V. Laitinen, L. B. N. Clausen, G. Facskó, A. Vaivads, H. E. J. Koskinen, I. Dandouras, H. Rème, and E. A. Lucek (2012), Supermagnetosonic subsolar magnetosheath jets and their effects: From the solar wind to the ionospheric convection, Ann. Geophys., 30, 33–48, doi:10.5194/angeo-30-33-2012.

Hietala, H., and F. Plaschke (2013), On the generation of magnetosheath high-speed jets by bow shock ripples, J. Geophys. Res. Space Physics, 118, 7237–7245, doi:10.1002/2013JA019172

Hietala, H., Phan, T. D., Angelopoulos, V., Oieroset, M., Archer, M. O., Karlsson, T., & Plaschke, F. (2018). In situ observations of a magnetosheath high-speed jet triggering magnetopause reconnection. Geophysical Research Letters, 45, 1732–1740. https://doi.org/10.1002/2017GL076525

Jarvinen, R., Vainio, R., Palmroth, M., Juusola, L., Hoilijoki, S., Pfau-Kempf, Y., … von Alfthan, S. (2018). Ion acceleration by flux transfer events in the terrestrial magnetosheath. Geophysical Research Letters, 45, 1723–1731. https://doi.org/10.1002/2017GL076192

Karimabadi, H., et al. (2014), The link between shocks, turbulence, and magnetic reconnection in collisionless plasmas, Phys. Plasmas, 21, 062308, doi:10.1063/1.4882875.

Liu, T. Z., H. Hietala, V. Angelopoulos, and D. L. Turner (2016), Observations of a new foreshock region upstream of a foreshock bubble’s shock, Geophys. Res. Lett., 43, 4708–4715, doi:10.1002/2016GL068984.

McFadden, J. P., C. W. Carlson, D. Larson, V. Angelopoulos, M. Ludlam, R. Abiad, B. Elliott, P. Turin, and M. Marckwordt (2008), The THEMIS ESA plasma instrument and in-flight calibration, Space Sci Rev., 141, 277–302, doi:10.1007/s11214-008-9440-2.

Merka, J., A. Szabo, J. A. Slavin, and M. Peredo (2005), Three-dimensional position and shape of the bow shock and their variation with upstream Mach numbers and interplanetary magnetic field orientation, J. Geophys. Res., 110 A04202, doi:10.1029/2004JA010944.

Omidi, N., J. Berchem, D. Sibeck, H. Zhang, Impacts of spontaneous hot flow anomalies on the magnetosheath and magnetopause. J. Geophys. Res. 121, 3155{3169 (2016). doi:10.1002/2015JA022170

Plaschke, F., H. Hietala, and V. Angelopoulos (2013), Anti-sunward high-speed jets in the subsolar magnetosheath, Ann. Geophys., 31(10), 1877–1889, doi:10.5194/angeo-31-1877-2013.

Plaschke, F., H. Hietala, V. Angelopoulos, and R. Nakamura (2016), Geoeffective jets impacting the magnetopause are very common, J. Geophys. Res. Space Physics, 121, 3240–3253, doi:10.1002/2016JA022534.

Plaschke, F., Hietala, H., Archer, M. et al. Space Sci Rev (2018) 214: 81. https://doi.org/10.1007/s11214-018-0516-3

Schwartz, S. J. (1998), Shock and discontinuity normal, Mach numbers, and related parameters, from Analysis Methods for Multi-Spacecraft Data, edited by G. Paschmann and P. W. Daly, pp. 249–270.

Sibeck, D. G., and V. Angelopoulos (2008), THEMIS science objectives and mission phases, Space Sci. Rev., doi:10.1007/s11214-008-9393-5.

Shue, J.-H., et al. (1998), Magnetopause location under extreme solar wind conditions, J. Geophys. Res., 103, 17

Sonnerup, B. U. O., and M. Scheible (1998), Minimum and maximum variance analysis, in Analysis Methods for Multi-Spacecraft Data, ISSI Sci. Rep. SR-001, edited by G. Paschmann and P. W. Daly, pp. 185–220, Eur. Space Agency Publ. Dif, Noordwijk, Netherlands.

Wang, B., Nishimura, Y., Hietala, H., Lyons, L., Angelopoulos, V., Plaschke, F., et al. (2018). Impacts of magnetosheath high-speed jets on the magnetosphere and ionosphere measured by optical imaging and satellite observations. Journal of Geophysical Research: Space Physics, 123, 4879–4894. https://doi.org/10.1029/2017JA024954